Enhanced exciton-to-trion conversion by proton irradiation of atomically thin WS2

Journal:	*Nano Letters*
Manuscript ID	nl-2022-04987c.R1
Manuscript Type:	Communication
Date Submitted by the Author:	08-Mar-2023

Complete List of Authors:	Wang, Xuejing; Los Alamos National Laboratory, Center for Integrated Nanotechnologies Pettes, Michael; Los Alamos National Laboratory, Center for Integrated Nanotechnologies, Materials Physics and Applications Division Wang, Yongqiang; Materials Physics and Applications Division, Zhu, Jian-Xin; Los Alamos National Laboratory, Theoretical Division Dhall, Rohan; E O Lawrence Berkeley National Laboratory, The Molecular Foundry Song, Chengyu; E O Lawrence Berkeley National Laboratory, National Center for Electron Microscopy Jones, Andrew; Los Alamos National Laboratory, MPA-CINT Ciston, Jim; E O Lawrence Berkeley National Laboratory, National Center for Electron Microscopy Yoo, Jinkyoung; Los Alamos National Laboratory, Center for Integrated Nanotechnologies

Enhanced exciton-to-trion conversion by proton irradiation of atomically thin WS_2

Xuejing Wang[1,*], Michael T. Pettes[1], Yongqiang Wang[1,2], Jian-Xin Zhu[1,3], Rohan Dhall[4], Chengyu Song[4], Andrew Crandall Jones[1], Jim Ciston[4], Jinkyoung Yoo[1,*]

[1] Center for Integrated Nanotechnologies (CINT), Los Alamos National Laboratory, Los Alamos, New Mexico 87545, U. S. A.

[2] Materials Science in Radiation and Dynamics Extremes (MST-8), Los Alamos National Laboratory, Los Alamos, New Mexico 87545, U. S. A.

[3] Physics of Condensed Matter and Complex Systems (T-4), Los Alamos National Laboratory, Los Alamos, New Mexico 87545, U. S. A.

[4] National Center for Electron Microscopy (NCEM), Molecular Foundry, Lawrence Berkeley National Laboratory, Berkeley, California 94720, U. S. A.

*Corresponding author, email: xuejing@lanl.gov, jyoo@lanl.gov

Defect engineering of van der Waals semiconductors has been demonstrated as an effective approach to manipulate the structural and functional characteristics toward dynamic device controls, yet correlations between physical properties with defect evolution remain underexplored. Here, using proton irradiation, we observe an enhanced exciton-to-trion conversion of the atomically thin WS_2. These altered excitonic states are found to be correlated with nanopore induced atomic displacement, W clusters and zigzag edge termination, which are verified by scanning transmission electron microscopy, photoluminescence, and Raman measurements. Density functional theory calculation suggests that nanopores facilitate the generation of in-gap states that provide sinks of free electrons to couple with excitons. The hypothesis of trion conversion mechanism is corroborated by our ion energy loss simulation, which predicts a dominant electron ionization effect with negligible atomic interactions, providing potential evidence on band perturbations and nanopore formation without destroying the overall crystallinity. This study provides a route in tuning the excitonic properties of van der Waals semiconductors using irradiation-based defect engineering approach.

Keywords: defect engineering, proton irradiation, nanopores, transition metal dichalcogenides (TMDs), excitonic property

Over the past decade, the emerging two-dimensional (2D) van der Waals (vdWs) materials has been implemented in practical applications such as flexible optoelectronics, spintronic devices, quantum computing, taking advantage of the unique characteristics such as spin-orbit coupling, tunable band structure that are capable of delivering unprecedented functionalities as compared to conventional bulk counterparts.[1-6] Along with progress in quantum science and physics such as twistronics, valleytronics and Majorana fermions, 2D optoelectronics such as transistors, photodetectors, light emitting diodes (LEDs), and single photon emitters have been developed showing outstanding performance.[7-20] Digging into the fundamental dynamics of excitonic states in vdWs materials such as trions, dark excitons, moiré excitons, or interlayer excitons provides fruitful insights in extending and tuning the material properties, as well as in building correlations between fundamental materials physics and devices.[21-23] Trions, the intrinsically charged quasi-particles composed of either two electrons and a hole (X^-), or two holes and an electron (X^+), enable transport and manipulation of excitons via external electric or magnetic field. Explorations of valley and spin dynamics as well as tunable binding energy of these tightly bound trions provide fundamental insights in many-body phenomena, programmable excitons, and novel optoelectronic devices.[24-27]

In terms of tuning the structure and properties, defect engineering has shown its effectiveness in vdWs semiconductors.[28-30] Thermal annealing, extrinsic doping, external stimuli such as strain, irradiation, are capable of generating multi-dimensional defects such as vacancies, dislocations, nanopores that effectively tune the stoichiometry, band structure, excitonic states, thus realizing controlled or extended electronic, optical or magnetic properties.[31-37] Irradiation with specific beam energy and fluence to impact 2D surfaces has been demonstrated as an effective defect engineering approach. For example, electron-beam irradiation has been conducted *in situ* inside a microscope column to explore the atomic displacement and live evolution of edge states.[38-40] Ion beam irradiation is considered as another approach to generate defects at industrially relevant length scales. Ion species such as swift heavy ions (e.g., Xe, Bi) or light ions (e.g. proton, He^+)[41, 42] along with other irradiation parameters such as beam energy, flux, fluence, temperature, and pressure can be controlled, resulting in changes of crystallinity, defect geometry, phase transformation and exciton emission.[39, 43-47] However, studies providing evidence on ion irradiation induced defects at atomic scale and their correlation with physical properties, e.g., excitonic states, are rare.

To unveil electronic and excitonic properties with defect evolution at the atomic level, we have performed proton irradiation with predefined energy and fluences across atomically thin (1~2 layers) tungsten disulfide (WS_2). By incorporating high-resolution photoluminescence (PL) mapping and scanning transmission electron microscopy (STEM), we have qualitatively demonstrated generation of nanopores that contributes to the dominating exciton-to-trion conversion. These nanopores modify local atomic rearrangements and create significant number of new edges, giving rise to lattice disorder and carrier redistribution, which are confirmed by our Kelvin probe force microscopy (KPFM), Raman shift measurements, and density functional theory (DFT) calculations. Our goal is to understand defect engineering and correlated changes of excitonic states, which plays a vital role in developing 2D optoelectronics with extendable and tunable device performance.

The exfoliated WS_2 flakes were dry transferred onto 285 nm amorphous (*a*-)SiO_2/Si (highly doped) substrates inside a glove box. A 100 keV proton beam with a moderate fluence of 10^{14} ions/cm^2 was carefully selected to ensure that the irradiation predominantly introduced mild defects from each ion strike with little chance of defects overlapping from different ions, and that the protons would be implanted far deep in the substrate. According to Stopping and Range of Ions in Matter (SRIM) estimation (Figure S1), ion energy loss to electronic ionizations/excitations is dominant in the 1L-WS_2 as compared to that to atomic displacements and phonon productions. Optical microscopy (OM) images (Figure 1a) of pristine (non-irradiated) and irradiated WS_2 suggest no noticeable change of contrast or microstructural damage to the material, both flakes appear clean and uniform coverage. Figure 1b shows the PL spectra of 1L-WS_2 at room temperature (RT) excited by 2.330 eV photons. Two features can be retrieved upon proton irradiation, i.e., quenching of the overall PL intensity with comparable peak linewidth, and a 14 meV redshift by comparing the major emission peak between pristine WS_2 and irradiated WS_2. These changes can be potentially correlated with generation of defect or disorder after being irradiated by the 100 keV proton beam, which will be discussed in more details.

Next, KPFM was performed to reveal the local work function of the pristine and irradiated WS_2 at the μm scale. Figure 1c,d displays the KPFM mapping at selected areas of pristine and irradiated 1L-WS_2 supported by the 285 nm *a*-SiO_2/Si substrate (marked rectangles in Figure 1a). Aside from the gaps introduced during sample preparation, the mapping indicates desirable homogeneity and uniform surface coverage without drastic variations in surface potential. The color contrast indicates a mild drop of contact potential difference (CPD) of WS_2 after proton irradiation, from which a lowered work function can be inferred.[48-50] Line profiles by integrating signals from the dashed area in Figure 1c,d are shown in Figure 1e,f. A general comparison reveals differences of CPD across the *a*-SiO_2/WS_2 lateral interface, 0.39 V for pristine sample, and 0.27 V for the proton irradiated sample (blue arrows). Interestingly, there is a gradual increase of CPD (cyan shades) from the edge towards the center of the WS_2 flake. We attribute this CPD variation to the redistribution or modification of the charge state of WS_2 upon irradiation, which is consistent with the quenched PL emission. We also noticed a pronounced drop at the irradiated *a*-SiO_2 surface close to the WS_2 edge (yellow shades), which may be originated from band bending along the interface between *a*-SiO_2 and WS_2 due to trapped charges upon irradiation.[51, 52]

To construct the emission property over the entire flake, PL mapping (Figure S2 shows area selection) with the excitation energy of 2.330 eV (532.3 nm) has been conducted on pristine and irradiated 1L-WS_2/*a*-SiO_2 at room temperature. Figure 2a-h display the OM images and corresponding maps of peak amplitude (counts/s), peak width (full width at half maximum, nm) and peak position (eV) for pristine and irradiated WS_2, by fitting the mapped spectra at 2.02 eV. Upon irradiation, there is a noticeable quenching of PL over the entire flake (Figure 2b,f), while still exhibits strong emission with uniform distribution. The peak width mapping (Figure 2c,g) indicates an ideal homogeneity within pristine WS_2, the minor variations of irradiated WS_2 could be caused by potential disorder or defect generation especially near edges or gaps (Figure S2c). Interestingly, from the peak position mapping (Figure 2d,h), there are lower-energy emissions in both pristine and irradiated WS_2, which could be explained by thickness variations due to folding or defects induced excitonic states near edges.[53] To identify the peak distribution, the integrated PL spectra from the mapped area are displayed in Figure 2i,j. Two major emissions, including the neutral exciton emission (X) at 2.019 eV and the trion emission (X^-) at 1.981 eV for the pristine flake, as well as X at 2.014 eV and X^- at 1.975 eV for the irradiated flake, have been identified using Lorentz peak deconvolution.[54] The weak trion emission from pristine WS_2 can be correlated with intrinsic defects such as sulfur (S) vacancies.[55] At the same scale, the intensities of the peaks reveal a noticeable increase of trion emission while a decrease of exciton emission after irradiation. Quantitatively, the X^-/X shows an increase from 0.142 (pristine) to 0.676 (irradiated), which provides direct evidence that the energy transfer from excitons to trions caused by irradiation is predominant as compared to the intrinsic S vacancy induced transfer.

The CPD variation (Figure 1f) suggests that the supporting *a*-SiO_2 layer potentially plays a role in affecting the local electronic property of WS_2.[56] Therefore, additional measurements were performed with WS_2 flakes transferred onto holey silicon nitride (SiN) TEM grids (200 nm-thick amorphous SiN (*a*-SiN) coated on 200 μm Si). PL of a free-standing pristine 1L-WS_2 is displayed separately in SI Figure S3, showing comparable peak positions and X^-/X ratio with features of supported pristine WS_2 (Figure 2i). Figure 3a shows a free-standing thin WS_2 flake after proton irradiation, containing both monolayer (1L) and bilayer (2L) regions. PL spectra were collected at RT and 4K, with the laser focus at the hole (green arrow). Interestingly, the X^-/X ratio maintains a comparable value between SiO_2 supported (0.676) and free-standing (0.708) WS_2 upon irradiation, indicating that the exciton-to-trion conversion is not significantly affected by the underlying substrate. whereas a significantly enhanced exciton-to-trion conversion, i.e., X^-/X increases from 0.708 (RT) to 3.122 (4K), suggests a more efficient trion conversion at cryogenic temperature.[57] It is noted that another broad emission peak located at lower energy (1.870 eV) could be assigned to the defect-bound state and/or background noise.[58, 59] At 4 K, we mapped the PL peak amplitude (counts/s), peak width (nm), and peak position (eV) for free-standing irradiated 1L-WS_2. The PL emission (Figure 3d) is majorly localized at two regions, i.e., WS_2/*a*-SiN (right) and WS_2/void (left) with slightly higher intensity, referring to the area as marked in Figure 3a. The peak width mapping (Figure 3e) of the 1L-WS_2 suggests a minor peak broadening of WS_2/void (left), which indicates more defects or disorder without supporting substrate. From the peak position mapping (Figure 3f), there is a sharp contrast between the free-standing (left) and supported (right) region, suggesting that the major emission peak (composed of X and X^-) of

WS_2/void shifts to the lower energy (redshift). It is inferred that proton irradiation induces more defects or electron interactions with the free-standing WS_2, correspondingly, more trions are formed by coupling excitons with free electrons. Temperature dependent PL and corresponding areal intensity maps (Figure S4) for 1L-WS_2/void indicate continuous redshift and attenuation for the major emissions, which have been consistently observed in monolayer TMDs.[60]

We summarized the room temperature Raman spectra of (A) pristine 1L-WS_2/*a*-SiO_2, (B) irradiated 1L-WS_2/*a*-SiO_2, (C) irradiated 1L-WS_2/*a*-SiN and (D) irradiated 1L-WS_2/void (free-standing) in Figure 3g. The major vibrational modes have been identified. Two first-order modes at the Brillouin zone center including $E^1_{2g}(\Gamma)$ and $A_{1g}(\Gamma)$, represent the in-plane displacement and the out-of-plane displacement (inset illustrations), respectively. The LA(M) mode belongs to the longitudinal acoustic mode that is activated by disorder.[61] A minor enhancement of LA(M) has been visualized for the irradiated 1L-WS_2 which indicates more disorder. The $E^1_{2g}(\Gamma)$ exhibits a slightly dropped intensity (Figure S5), which can be interpreted as less active in-plane interactions upon irradiation. The remaining peaks, including the longitudinal optical (LO) mode of Si (Figure S6), appear to be comparable without noticeable changes. Obvious enhancement for LA modes and the $A_{1g}(\Gamma)$ modes (red arrows) have been observed in irradiated 1L-WS_2/void, which indicates defect induced disorder and out-of-plane atomic displacement could be more pronounced without supporting substrate. But in between the two spectra there is no observable lateral shift of these active Raman modes.[61, 62].

The atomic structure of the free-standing irradiated WS_2 was probed by aberration-corrected high-angle annular dark field (AC-HAADF) STEM to unveil defect morphology. Raw images at low magnification can be found in Figure S7, where a wide distribution of nanopores have been observed over the entire irradiated 1L-WS_2, resulting in approximately 22% area fraction. The high-resolution STEM (HRSTEM) micrographs were processed to filter out background and detector noise. Figure 4a-d display the local atomic stacking close to the nanopores, where a few interesting features, represented by agglomeration of W atoms (brighter contrast) forming dangling nanoclusters inside the nanopores, as well as folded W–W stacking at the pore edges, have been identified. Away from the pores, multiple W vacancies and W–W folding can be traced as marked by green arrows and dashed circles. Lattice disorder, majorly located at the pore edges where atomic displacements break the original hexagonal symmetry, has been confirmed by our hypothesis on the enhanced LA(M) and $A_{1g}(\Gamma)$ Raman modes. Reported studies suggest that (heavy) ion bombardment induces sputtering of S atoms out of covalent bonded S–Mo–S, forming S vacancies and/or Mo displacement. [41, 63, 64] Our SRIM simulation (Figure S1) indicates a mild atomic sputtering effect upon proton irradiation which contributes to the nanopore formation without breaking the overall lattice integrity, but the underlying mechanism could be more sophisticated. Figure 4e shows a bilayer region where the bonding between W and S atoms can be identified. The two individual nanopores only occur at the top 1L-WS_2 while the bottom monolayer remains intact, potentially indicating that our proton irradiation recipe is effective in defect generation with controlled ion–matter interaction. The zoomed atomic micrograph (Figure 4f) away from the nanopore shows a hexagonal stacking that matches well with the perfect WS_2 model. It is worth noting that atomic termination (e.g., zigzag or armchair) at the edge is known to affect the local electronic properties.[65, 66] Here, we found that the imaged nanopores (Figure 4g) exhibit a zigzag alignment with W exposure at the long edges as marked by the overlaid atomic model. Overall, the coalescence of nanopores generate a series of defects: S vacancies, W vacancies, W nanoclusters and W-W folding (disorder), broken lattice symmetry at the edges (disorder), and zigzag edge exposure. More HRSTEM micrographs collected at different sample regions are displayed in Figure S8.

It is noted that W clusters will not contribute to the change of photoluminescence due to their metallic nature. Therefore, by excluding the disorder related defects (W cluster, and W-W folding) and rather randomly reoriented lattices at the edges which is too sophisticated to predict, the remaining defects that could affect the local electronic band structure would be W (less common)/S vacancies, zigzag W edge, and nanopore itself. We then performed DFT calculations of the density of states (DOS) mimicking each defect type to predict the changes of band gap behavior. Figure 4h-j displays a DOS plot for three major types, including a perfect monolayer WS_2, monolayer WS_2 with a single S vacancy, a nanopore and a zigzag W edge. Additional calculations and atomic models are summarized in Figure S9. Perfect 1L-WS_2 without defects shows a typical band gap of 1.3 eV, whereas calculated DOS of defect contained 1L-WS_2 exhibit generation of an in-gap state, represented by the yellow shaded region. Although S vacancy is not the highlighted defect type, we intended to include it because it is known that the chalcogen vacancies of as-grown or engineered TMDs play a role in changing the emission properties, which is the origin of our observed trion peak from both pristine and irradiated 1L-WS_2/*a*-SiO_2 (Figure 2i).[67]

To explain the mechanism of trion emission affected by defects, electronic band structures are illustrated in Figure 4h-j (insets). Perfect 1L-WS_2 and energy required to excite exciton (electron-hole pair, e-h) and trion (e-h-e) are shown in different colors. By generating S vacancies within 1L-WS_2, a small in-gap state could provide a sink for free electrons, which allows excitons to be coupled with these electrons to form trions at a lower energy. When nanopores are introduced, we could expect that the in-gap state further narrows the band gap and induce band perturbations, which facilitate free carriers coupling with excitons, thus enabling an enhanced exciton-to-trion conversion. These predictions are corroborated by our SRIM simulations in terms of proton induced electronic ionizations/excitations. As compared to S vacancy induced trion emission, we want to clarify that the nanopore induced trion emission is more dominating, as evidenced by the PL spectra in Figure 2(i,j). Considering the entire flake of which 22% area is covered with nanopores, we could imagine 146% increase in the edge length, which significantly alters the electronic and optical properties. Compare to nanopore generation using thermal annealing, laser injection, or *in situ* electron beam injection,[34, 68, 69] proton irradiation induces formation of nanopores in wafer scale within a few minutes, while the crystallinity of the material is still maintained. Potential interactions such as atomic displacement, strained bonds (Si–O or Si–N), or trapped charges with the supporting substrate are minimized at our selected energy and doses of proton injection to ensure that the observed change of excitonic properties are mainly originated from the atomically thin WS_2 layer.[70, 71] Although generation of nanopores with broken lattice symmetry degrades the overall integrity or homogeneity, proton irradiation as demonstrated here can be considered as an effective defect engineering method to manipulate excitonic properties of 2D semiconductors and could potentially realize emergence of physical properties such as ferromagnetism.[36, 72, 73]

To summarize, we have demonstrated that proton irradiation serves as an effective defect engineering method to introduce nanopores that can be correlated with tuning of physical properties. We highlight the photoluminescence mapping for both *a*-SiO_2/Si supported and free-standing WS_2 monolayers to demonstrate interesting observations represented by enhanced exciton-to-trion conversion without deteriorating the material homogeneity or crystallinity. The nanopores have been clearly observed at atomic resolution, and density of states calculations based on defects including vacancies, nanopore and zigzag edge termination suggest the generation of in-gap states that explain the enhanced trion formation. In general, these defects are intercorrelated and collaboratively modify the optical and electronic properties. Future directions are open to realizing controllable generation of defects and understanding the evolution of atomic structure at the pore edges upon irradiation, such that the exact energy level of excitonic states can be predicted precisely by defect engineering approach. Our results support fundamental materials physics toward developing tunable 2D electronic and spintronic devices.

Sample Preparation. Monolayer WS_2 flakes were prepared using mechanical exfoliation by scotch tape method. 2H-WS_2 crystals (>99.995% purity, $a = b = 0.315$ nm, $c = 1.227$ nm) were purchased from HQ graphene. WS_2 flakes were first exfoliated on polydimethylsiloxane (PDMS) films sticked on glass slides at ambient atmosphere, and then transferred onto 285 nm *a*-SiO_2/Si (highly doped Si for conduction) substrates using the transfer system (HQ Graphene) inside the glove box. PELCO SiN grids, with 0.1×0.1 mm^2 windows with hole dimensions of 1.25 μm, were applied for free-standing transfer. The grids are composed of 200 nm-thick amorphous SiN film grown on 200 μm Si wafer. The specimen viewing area is created by etching away a window in the silicon wafer substrate underneath the SiN membrane, leaving a perfectly smooth, resilient, and chemically robust SiN film (8 nm).

Proton Irradiation. 100 keV proton beam irradiation was carried out on 200 kV Danfysik Research Implanter at the Ion Beam Materials Laboratory in Los Alamos National Laboratory. The irradiation was performed under room temperature with a fluence of 10^{14} ions/cm^2, a beam flux of approximately 10^{13} ions/cm^2/s. The target chamber was maintained under vacuum of 6×10^{-7} torr during the irradiation. A thermocouple attached on the copper sample stage indicated no appreciable temperature change above room temperature. 100 keV energy was chosen to ensure that only simple point defects were generated within the specimens (no protons stopped in the specimens as unwanted hydrogen doping impurities) and within the implanter's optimum operating energy range.

Optical Characterization. Photoluminescence and Raman spectroscopic measurements were conducted in reflection mode using 532.3 nm continuous wave excitation (100 mW, Oxxius LCX-532S-100, CW single longitudinal mode diode pumped solid state laser), in a Horiba LabRAM HR Evolution high resolution confocal PL/Raman microscope fitted with volume Bragg gratings. The sample temperature was controlled by a continuous flow cryostat (MicrostatHiRes variable temperature optical cryostat system, Oxford Instruments). PL was measured using a 600 mm^{-1} holographic grating blazed at 500 nm and a 300-700 mm confocal hole diameter, and either a 60×, 0.7 N.A. cover glass-corrected objective (cryostat) or a 100×, 0.9 N.A. objective (ambient). Raman experiments were configured using a 2400 mm^{-1} holographic grating blazed at 250 nm, a 50 μm confocal hole diameter. Spectral calibration was performed using the 1332.5 cm^{-1} band of a synthetic Type IIa diamond[74], and spectral intensity was calibrated using a VIS-halogen light source (NIST test no. 685/289682-17). Instrumental linewidth broadening was measured using a Hg(Ar) spectral calibration lamp (Oriel 6035) to be ~0.9 cm^{-1} in the configuration used here.

Kelvin Probe Force Microscopy (KPFM). The measurement was conducted at room temperature and ambient atmosphere using Bruker Dimension Icon atomic force microscopy (AFM) system. The work function mapping was performed in PeakForce Tapping mode using highly doped Si (PFQNE-AL) tips. A topography scan with a feedback force deflection setpoint of 7.99 nN was first used to map the height variation of the sample. The AFM probe was subsequently lifted to a height of 40 nm above the surface and retraced over the sample. During this lift mode trace, the KPFM feedback was performed utilizing a direct current (DC) bias voltage applied to the sample to minimize frequency sidebands resulting from the mixing of mechanical oscillations of the probe

(~300 kHz) and an 5V alternating current (AC) potential applied to the sample at a frequency of 2 kHz. The contact potential difference (CPD) is related to the work function (WF) between the tip and sample $V_{CPD}(mV) = (WF_{sample} - WF_{tip})/q$ where q is elementary charge unit. The measurements for all samples were conducted using the same alignment and tip to avoid instrumental and environmental variations.

Scanning Transmission Electron Microscopy (STEM). A double-aberration-corrected scanning transmission electron microscope (TEAM I), i.e., a modified FEI Titan 80-300 microscope equipped with a high-brightness Schottky-field emission "X-FEG" electron source, was applied for high-angle annular dark field (HAADF) STEM imaging with an accelerating voltage of 80kV. HRSTEM image processing (color coding and filtering) was completed based on openNCEM package (developed by scientists at National Center for Electron Microscopy and accessible through GitHub, https://github.com/ercius/openNCEM).

DFT calculation. Density functional theory (DFT) based first-principles electronic structure calculations were carried out by using the pseudopotential projector-augmented wave method implemented in the Vienna ab initio simulation package (VASP).[75] We used an energy cutoff of 500 eV for the plane-wave basis set. Exchange-correlation effects were treated using the Perdew-Burke-Ernzerhof (PBE) Generalized Gradient Approximation (GGA) density functional. Spin-orbit coupling effects were included self-consistently. Starting with a single layer WS_2, the following cases were considered: a single-W vacancy (in a $4 \times 4 \times 1$ supercell); a single-S vacancy (in a $4 \times 4 \times 1$ supercell), a pinhole of the size of 18 WS_2 formula units (in a $12 \times 12 \times 1$ supercell), and both armchair and zigzag edge strip of the width of about 80 Å (rectangular unit cell). Except for the pinhole structure, for which the calculation was with Γ point, the first Brillouin zone sampling was performed with Monkhorst-Pack (MP) Γ-centered 8×8 (single-atom vacancy), and $12 \times 12 \times 1$ (armchair strip) and 20×20×1 (zigzag strip) k-point meshes. The self-consistent simulations used a total energy tolerance of 10^{-7} eV for convergence. We note that for the zigzag structure, edge ferromagnetism was reported for MoS_2 and WS_2. In our calculations, only nonmagnetism was considered for the sole purpose to study the low-energy electronic states. In addition, the PBE GGA underestimates the band gap is a known fact. However, it does not change our conclusion on the existence of in-gap electronic states at vacancies or edges.

Supporting Information

(1) SRIM simulation of proton irradiation. Ion energy loss profile of $WS_2/SiO_2/Si$ and WS_2/SiN/Si. (2) Room temperature PL of a pristine free-standing 1L-WS_2 flake. (3) Temperature dependent PL of the irradiated free-standing 1L-WS_2. (4) Raman results. (5) Additional HAADF STEM micrographs of irradiated WS_2. (6) Atomic models for defect contained 1L-WS_2 and additional DOS profile.

Acknowledgement

This work was supported by the Laboratory Directed Research and Development program of Los Alamos National Laboratory under project numbers 20210965PRD4, 20210782ER 20210640ECR, and an Institute for Materials Science Rapid Response Award. This work was performed in part at the Center for Integrated Nanotechnologies, an Office of Science User Facility operated for the U.S. Department of Energy (DOE) Office of Science. Los Alamos National Laboratory, an affirmative action equal opportunity employer, is managed by Triad National Security, LLC for the U.S. Department of Energy's NNSA, under contract 89233218CNA000001.

Transmission electron microscopy work at the Molecular Foundry was supported by the Office of Science, Office of Basic Energy Sciences, of the U.S. Department of Energy under Contract no. DE-AC02-05CH11231. We acknowledge NERSC and LANL IC Programs for computational resources.

References

(1) Manzeli, S.; Ovchinnikov, D.; Pasquier, D.; Yazyev, O. V. Kis, A. 2D transition metal dichalcogenides. *Nat. Rev. Mater.* **2017,** *2*, 17033.

(2) Sierra, J. F.; Fabian, J.; Kawakami, R. K.; Roche, S. Valenzuela, S. O. Van der Waals heterostructures for spintronics and opto-spintronics. *Nat. Nanotechnol.* **2021,** *16*, 856.

(3) Choi, E.-M.; Sim, K. I.; Burch, K. S. Lee, Y. H. Emergent Multifunctional Magnetic Proximity in van der Waals Layered Heterostructures. *Adv. Sci.* **2022,** *9*, 2200186.

(4) Liu, X. Hersam, M. C. 2D materials for quantum information science. *Nat. Rev. Mater.* **2019,** *4*, 669.

(5) Xia, F.; Wang, H.; Xiao, D.; Dubey, M. Ramasubramaniam, A. Two-dimensional material nanophotonics. *Nat. Photon.* **2014,** *8*, 899.

(6) Akinwande, D.; Petrone, N. Hone, J. Two-dimensional flexible nanoelectronics. *Nat. Commun.* **2014,** *5*, 5678.

(7) Berkelbach, T. C.; Hybertsen, M. S. Reichman, D. R. Theory of neutral and charged excitons in monolayer transition metal dichalcogenides. *Phys. Rev. B* **2013,** *88*, 045318.

(8) Schaibley, J. R.; Yu, H.; Clark, G.; Rivera, P.; Ross, J. S.; Seyler, K. L.; Yao, W. Xu, X. Valleytronics in 2D materials. *Nat. Rev. Mater.* **2016,** *1*, 16055.

(9) Liu, Y.; Duan, X.; Shin, H.-J.; Park, S.; Huang, Y. Duan, X. Promises and prospects of two-dimensional transistors. *Nature* **2021,** *591*, 43.

(10) Lopez-Sanchez, O.; Lembke, D.; Kayci, M.; Radenovic, A. Kis, A. Ultrasensitive photodetectors based on monolayer MoS2. *Nat. Nanotechnol.* **2013,** *8*, 497.

(11) Zhang, Y. J.; Oka, T.; Suzuki, R.; Ye, J. T. Iwasa, Y. Electrically Switchable Chiral Light-Emitting Transistor. *Science* **2014,** *344*, 725.

(12) Mak, K. F. Shan, J. Photonics and optoelectronics of 2D semiconductor transition metal dichalcogenides. *Nat. Photon.* **2016,** *10*, 216.

(13) Liao, M.; Wei, Z.; Du, L.; Wang, Q.; Tang, J.; Yu, H.; Wu, F.; Zhao, J.; Xu, X.; Han, B.; Liu, K.; Gao, P.; Polcar, T.; Sun, Z.; Shi, D.; Yang, R. Zhang, G. Precise control of the interlayer twist angle in large scale MoS2 homostructures. *Nat. Commun.* **2020,** *11*, 2153.

(14) Zhao, H.; Pettes, M. T.; Zheng, Y. Htoon, H. Site-controlled telecom-wavelength single-photon emitters in atomically-thin $MoTe_2$. *Nat. Commun.* **2021,** *12*, 6753.

(15) Wu, W.; Dass, C. K.; Hendrickson, J. R.; Montaño, R. D.; Fischer, R. E.; Zhang, X.; Choudhury, T. H.; Redwing, J. M.; Wang, Y. Pettes, M. T. Locally defined quantum emission from epitaxial few-layer tungsten diselenide. *Appl. Phys. Lett.* **2019,** *114*, 213102.

(16) Branny, A.; Kumar, S.; Proux, R. Gerardot, B. D. Deterministic strain-induced arrays of quantum emitters in a two-dimensional semiconductor. *Nat. Commun.* **2017,** *8*, 15053.

(17) Tran, T. T.; Bray, K.; Ford, M. J.; Toth, M. Aharonovich, I. Quantum emission from hexagonal boron nitride monolayers. *Nat. Nanotechnol.* **2016,** *11*, 37.

(18) Palacios-Berraquero, C.; Barbone, M.; Kara, D. M.; Chen, X.; Goykhman, I.; Yoon, D.; Ott, A. K.; Beitner, J.; Watanabe, K.; Taniguchi, T.; Ferrari, A. C. Atatüre, M. Atomically thin quantum light-emitting diodes. *Nat. Commun.* **2016,** *7*, 12978.

(19) He, Y.-M.; Clark, G.; Schaibley, J. R.; He, Y.; Chen, M.-C.; Wei, Y.-J.; Ding, X.; Zhang, Q.; Yao, W.; Xu, X.; Lu, C.-Y. Pan, J.-W. Single quantum emitters in monolayer semiconductors. *Nat. Nanotechnol.* **2015,** *10*, 497.

(20) Chakraborty, C.; Kinnischtzke, L.; Goodfellow, K. M.; Beams, R. Vamivakas, A. N. Voltage-controlled quantum light from an atomically thin semiconductor. *Nat. Nanotechnol.* **2015,** *10*, 507.

(21) Mueller, T. Malic, E. Exciton physics and device application of two-dimensional transition metal dichalcogenide semiconductors. *npj 2D Mater. Appl.* **2018,** *2*, 29.

(22) Wilson, N. P.; Yao, W.; Shan, J. Xu, X. Excitons and emergent quantum phenomena in stacked 2D semiconductors. *Nature* **2021,** *599*, 383.

(23) Plechinger, G.; Nagler, P.; Arora, A.; Schmidt, R.; Chernikov, A.; del Águila, A. G.; Christianen, P. C. M.; Bratschitsch, R.; Schüller, C. Korn, T. Trion fine structure and coupled spin–valley dynamics in monolayer tungsten disulfide. *Nat. Commun.* **2016,** *7*, 12715.

(24) Yang, J.; Xu, R.; Pei, J.; Myint, Y. W.; Wang, F.; Wang, Z.; Zhang, S.; Yu, Z. Lu, Y. Optical tuning of exciton and trion emissions in monolayer phosphorene. *Light Sci. Appl.* **2015,** *4*, e312.

(25) Duan, J.; Chava, P.; Ghorbani-Asl, M.; Erb, D.; Hu, L.; Krasheninnikov, A. V.; Schneider, H.; Rebohle, L.; Erbe, A.; Helm, M.; Zeng, Y.-J.; Zhou, S. Prucnal, S. Enhanced Trion Emission in Monolayer MoSe2 by Constructing a Type-I Van Der Waals Heterostructure. *Adv. Funct. Mater.* **2021,** *31*, 2104960.

(26) Mak, K. F.; He, K.; Lee, C.; Lee, G. H.; Hone, J.; Heinz, T. F. Shan, J. Tightly bound trions in monolayer MoS2. *Nat. Mater.* **2013,** *12*, 207.

(27) Singh, A.; Moody, G.; Tran, K.; Scott, M. E.; Overbeck, V.; Berghäuser, G.; Schaibley, J.; Seifert, E. J.; Pleskot, D.; Gabor, N. M.; Yan, J.; Mandrus, D. G.; Richter, M.; Malic, E.; Xu, X. Li, X. Trion formation dynamics in monolayer transition metal dichalcogenides. *Phys. Rev. B* **2016,** *93*, 041401.

(28) Lin, Z.; Carvalho, B. R.; Kahn, E.; Lv, R.; Rao, R.; Terrones, H.; Pimenta, M. A. Terrones, M. Defect engineering of two-dimensional transition metal dichalcogenides. *2D Mater.* **2016,** *3*, 022002.

(29) Liang, Q.; Zhang, Q.; Zhao, X.; Liu, M. Wee, A. T. S. Defect Engineering of Two-Dimensional Transition-Metal Dichalcogenides: Applications, Challenges, and Opportunities. *ACS Nano* **2021,** *15*, 2165.

(30) Patra, T. K.; Zhang, F.; Schulman, D. S.; Chan, H.; Cherukara, M. J.; Terrones, M.; Das, S.; Narayanan, B. Sankaranarayanan, S. K. R. S. Defect Dynamics in 2-D MoS2 Probed by Using Machine Learning, Atomistic Simulations, and High-Resolution Microscopy. *ACS Nano* **2018,** *12*, 8006.

(31) Tongay, S.; Suh, J.; Ataca, C.; Fan, W.; Luce, A.; Kang, J. S.; Liu, J.; Ko, C.; Raghunathanan, R.; Zhou, J.; Ogletree, F.; Li, J.; Grossman, J. C. Wu, J. Defects activated photoluminescence in two-dimensional semiconductors: interplay between bound, charged and free excitons. *Sci. Rep.* **2013,** *3*, 2657.

(32) Cui, Q.; Luo, Z.; Cui, Q.; Zhu, W.; Shou, H.; Wu, C.; Liu, Z.; Lin, Y.; Zhang, P.; Wei, S.; Yang, H.; Chen, S.; Pan, A. Song, L. Robust and High Photoluminescence in WS2 Monolayer through In Situ Defect Engineering. *Adv. Funct. Mater.* **2021,** *31*, 2105339.

(33) Sang, X.; Li, X.; Zhao, W.; Dong, J.; Rouleau, C. M.; Geohegan, D. B.; Ding, F.; Xiao, K. Unocic, R. R. In situ edge engineering in two-dimensional transition metal dichalcogenides. *Nat. Commun.* **2018,** *9*, 2051.

(34) Danda, G.; Masih Das, P. Drndić, M. Laser-induced fabrication of nanoporous monolayer WS ₂ membranes. *2D Mater.* **2018,** *5*, 035011.

(35) Ke, J.-A.; Garaj, S. Gradečak, S. Nanopores in 2D MoS2: Defect-Mediated Formation and Density Modulation. *ACS Appl. Mater. Interfaces* **2019,** *11*, 26228.

(36) Huo, N.; Li, Y.; Kang, J.; Li, R.; Xia, Q. Li, J. Edge-states ferromagnetism of WS2 nanosheets. *Appl. Phys. Lett.* **2014,** *104*, 202406.

(37) Li, H.; Tsai, C.; Koh, A. L.; Cai, L.; Contryman, A. W.; Fragapane, A. H.; Zhao, J.; Han, H. S.; Manoharan, H. C.; Abild-Pedersen, F.; Nørskov, J. K. Zheng, X. Activating and optimizing MoS2 basal planes for hydrogen evolution through the formation of strained sulphur vacancies. *Nat. Mater.* **2016,** *15*, 48.

(38) Lehnert, T.; Lehtinen, O.; Algara–Siller, G. Kaiser, U. Electron radiation damage mechanisms in 2D MoSe2. *Appl. Phys. Lett.* **2017,** *110*, 033106.

(39) Madauß, L.; Ochedowski, O.; Lebius, H.; Ban-d'Etat, B.; Naylor, C. H.; Johnson, A. T. C.; Kotakoski, J. Schleberger, M. Defect engineering of single- and few-layer MoS ₂ by swift heavy ion irradiation. *2D Mater.* **2016,** *4*, 015034.

(40) Lin, Y.-C.; Dumcenco, D. O.; Huang, Y.-S. Suenaga, K. Atomic mechanism of the semiconducting-to-metallic phase transition in single-layered MoS2. *Nat. Nanotechnol.* **2014,** *9*, 391.

(41) He, Z.; Zhao, R.; Chen, X.; Chen, H.; Zhu, Y.; Su, H.; Huang, S.; Xue, J.; Dai, J.; Cheng, S.; Liu, M.; Wang, X. Chen, Y. Defect Engineering in Single-Layer MoS2 Using Heavy Ion Irradiation. *ACS Appl. Mater. Interfaces* **2018,** *10*, 42524.

(42) Krasheninnikov, A. V. Are two-dimensional materials radiation tolerant? *Nanoscale Horiz.* **2020,** *5*, 1447.

(43) Schwestka, J.; Inani, H.; Tripathi, M.; Niggas, A.; McEvoy, N.; Libisch, F.; Aumayr, F.; Kotakoski, J. Wilhelm, R. A. Atomic-Scale Carving of Nanopores into a van der Waals Heterostructure with Slow Highly Charged Ions. *ACS Nano* **2020,** *14*, 10536.

(44) Klein, J.; Kuc, A.; Nolinder, A.; Altzschner, M.; Wierzbowski, J.; Sigger, F.; Kreupl, F.; Finley, J. J.; Wurstbauer, U.; Holleitner, A. W. Kaniber, M. Robust valley polarization of helium ion modified atomically thin MoS ₂. *2D Mater.* **2017,** *5*, 011007.

(45) Thiruraman, J. P.; Fujisawa, K.; Danda, G.; Das, P. M.; Zhang, T.; Bolotsky, A.; Perea-López, N.; Nicolaï, A.; Senet, P.; Terrones, M. Drndić, M. Angstrom-Size Defect Creation and Ionic Transport through Pores in Single-Layer MoS2. *Nano Lett.* **2018,** *18*, 1651.

(46) Wang, B.; Yang, S.; Chen, J.; Mann, C.; Bushmaker, A. Cronin, S. B. Radiation-induced direct bandgap transition in few-layer MoS2. *Appl. Phys. Lett.* **2017,** *111*, 131101.

(47) Chen, Y.; Huang, S.; Ji, X.; Adepalli, K.; Yin, K.; Ling, X.; Wang, X.; Xue, J.; Dresselhaus, M.; Kong, J. Yildiz, B. Tuning Electronic Structure of Single Layer MoS2 through Defect and Interface Engineering. *ACS Nano* **2018,** *12*, 2569.

(48) Hu, Z.; Avila, J.; Wang, X.; Leong, J. F.; Zhang, Q.; Liu, Y.; Asensio, M. C.; Lu, J.; Carvalho, A.; Sow, C. H. Castro Neto, A. H. The Role of Oxygen Atoms on Excitons at the Edges of Monolayer WS2. *Nano Lett.* **2019,** *19*, 4641.

(49) Wang, X.; Dan, J.; Hu, Z.; Leong, J. F.; Zhang, Q.; Qin, Z.; Li, S.; Lu, J.; Pennycook, S. J.; Sun, W. Sow, C. H. Defect Heterogeneity in Monolayer WS2 Unveiled by Work Function Variance. *Chem. Mater.* **2019,** *31*, 7970.

(50) Alexeev, E. M.; Mullin, N.; Ares, P.; Nevison-Andrews, H.; Skrypka, O.; Godde, T.; Kozikov, A.; Hague, L.; Wang, Y.; Novoselov, K. S.; Fumagalli, L.; Hobbs, J. K. Tartakovskii, A. I. Emergence of Highly Linearly Polarized Interlayer Exciton Emission in MoSe2/WSe2 Heterobilayers with Transfer-Induced Layer Corrugation. *ACS Nano* **2020,** *14*, 11110.

(51) Schwank, J. R.; Shaneyfelt, M. R.; Fleetwood, D. M.; Felix, J. A.; Dodd, P. E.; Paillet, P. Ferlet-Cavrois, V. Radiation Effects in MOS Oxides. *IEEE Trans. Nucl. Sci.* **2008,** *55*, 1833.

(52) Wang, H.; Ren, D.; Lu, C. Yan, X. Investigation of multilayer WS2 flakes as charge trapping stack layers in non-volatile memories. *Appl. Phys. Lett.* **2018,** *112*, 231903.

(53) Kastl, C.; Koch, R. J.; Chen, C. T.; Eichhorn, J.; Ulstrup, S.; Bostwick, A.; Jozwiak, C.; Kuykendall, T. R.; Borys, N. J.; Toma, F. M.; Aloni, S.; Weber-Bargioni, A.; Rotenberg, E.

Schwartzberg, A. M. Effects of Defects on Band Structure and Excitons in WS2 Revealed by Nanoscale Photoemission Spectroscopy. *ACS Nano* **2019,** *13*, 1284.

(54) Plechinger, G.; Nagler, P.; Kraus, J.; Paradiso, N.; Strunk, C.; Schüller, C. Korn, T. Identification of excitons, trions and biexcitons in single-layer WS2. *Phys. Status Solidi - Rapid Res. Lett.* **2015,** *9*, 457.

(55) Zhou, W.; Zou, X.; Najmaei, S.; Liu, Z.; Shi, Y.; Kong, J.; Lou, J.; Ajayan, P. M.; Yakobson, B. I. Idrobo, J.-C. Intrinsic Structural Defects in Monolayer Molybdenum Disulfide. *Nano Lett.* **2013,** *13*, 2615.

(56) Florian, M.; Hartmann, M.; Steinhoff, A.; Klein, J.; Holleitner, A. W.; Finley, J. J.; Wehling, T. O.; Kaniber, M. Gies, C. The Dielectric Impact of Layer Distances on Exciton and Trion Binding Energies in van der Waals Heterostructures. *Nano Lett.* **2018,** *18*, 2725.

(57) Cuadra, J.; Baranov, D. G.; Wersäll, M.; Verre, R.; Antosiewicz, T. J. Shegai, T. Observation of Tunable Charged Exciton Polaritons in Hybrid Monolayer WS2−Plasmonic Nanoantenna System. *Nano Lett.* **2018,** *18*, 1777.

(58) Zhang, S.; Hu, P.; Xu, L.; Chen, H.; Maaz, K.; Zhai, P.; Li, Z.; Liu, L.; Ai, W.; Zeng, J. Liu, J. Exciton Transitions in Monolayer WS2 Activated by Swift Heavy Ion Irradiation. *J. Phys. Chem. C* **2021,** *125*, 20389.

(59) Wang, Y.; Deng, L.; Wei, Q.; Wan, Y.; Liu, Z.; Lu, X.; Li, Y.; Bi, L.; Zhang, L.; Lu, H.; Chen, H.; Zhou, P.; Zhang, L.; Cheng, Y.; Zhao, X.; Ye, Y.; Huang, W.; Pennycook, S. J.; Loh, K. P. Peng, B. Spin-Valley Locking Effect in Defect States of Monolayer MoS2. *Nano Lett.* **2020,** *20*, 2129.

(60) Huang, J.; Hoang, T. B. Mikkelsen, M. H. Probing the origin of excitonic states in monolayer WSe2. *Sci. Rep.* **2016,** *6*, 22414.

(61) Berkdemir, A.; Gutiérrez, H. R.; Botello-Méndez, A. R.; Perea-López, N.; Elías, A. L.; Chia, C.-I.; Wang, B.; Crespi, V. H.; López-Urías, F.; Charlier, J.-C.; Terrones, H. Terrones, M. Identification of individual and few layers of WS2 using Raman Spectroscopy. *Sci. Rep.* **2013,** *3*, 1755.

(62) Li, H.; Zhang, Q.; Yap, C. C. R.; Tay, B. K.; Edwin, T. H. T.; Olivier, A. Baillargeat, D. From Bulk to Monolayer MoS2: Evolution of Raman Scattering. *Adv. Funct. Mater.* **2012,** *22*, 1385.

(63) Huang, B.; Tian, F.; Shen, Y.; Zheng, M.; Zhao, Y.; Wu, J.; Liu, Y.; Pennycook, S. J. Thong, J. T. L. Selective Engineering of Chalcogen Defects in MoS2 by Low-Energy Helium Plasma. *ACS Appl. Mater. Interfaces* **2019,** *11*, 24404.

(64) Mignuzzi, S.; Pollard, A. J.; Bonini, N.; Brennan, B.; Gilmore, I. S.; Pimenta, M. A.; Richards, D. Roy, D. Effect of disorder on Raman scattering of single-layer $\mathrm{Mo}{\mathrm{S}}_{2}$. *Phys. Rev. B* **2015,** *91*, 195411.

(65) Rostami, H.; Asgari, R. Guinea, F. Edge modes in zigzag and armchair ribbons of monolayer MoS2. *J. Phys. Condens. Matter* **2016,** *28*, 495001.

(66) Kobayashi, Y.; Fukui, K.-i.; Enoki, T.; Kusakabe, K. Kaburagi, Y. Observation of zigzag and armchair edges of graphite using scanning tunneling microscopy and spectroscopy. *Phys. Rev. B* **2005,** *71*, 193406.

(67) Mitterreiter, E.; Schuler, B.; Micevic, A.; Hernangómez-Pérez, D.; Barthelmi, K.; Cochrane, K. A.; Kiemle, J.; Sigger, F.; Klein, J.; Wong, E.; Barnard, E. S.; Watanabe, K.; Taniguchi, T.; Lorke, M.; Jahnke, F.; Finley, J. J.; Schwartzberg, A. M.; Qiu, D. Y.; Refaely-Abramson, S.; Holleitner, A. W.; Weber-Bargioni, A. Kastl, C. The role of chalcogen vacancies for atomic defect emission in MoS2. *Nat. Commun.* **2021,** *12*, 3822.

(68) Chen, J.; Ryu, G. H.; Zhang, Q.; Wen, Y.; Tai, K.-L.; Lu, Y. Warner, J. H. Spatially Controlled Fabrication and Mechanisms of Atomically Thin Nanowell Patterns in Bilayer WS2 Using in Situ High Temperature Electron Microscopy. *ACS Nano* **2019,** *13*, 14486.

(69) Gerkman, M. A.; Lee, J. K.; Li, X.; Zhang, Q.; Windley, M.; Fonseca, M. V.; Lu, Y.; Warner, J. H. Han, G. G. D. Direct Imaging of Individual Molecular Binding to Clean Nanopore Edges in 2D Monolayer MoS2. *ACS Nano* **2020,** *14*, 153.

(70) Devine, R. A. B. Macroscopic and microscopic effects of radiation in amorphous SiO2. *Nucl. Instrum. Methods Phys. Res. B* **1994,** *91*, 378.

(71) EerNisse, E. P. Norris, C. B. Introduction rates and annealing of defects in ion-implanted SiO2 layers on Si. *J. Appl. Phys.* **1974,** *45*, 5196.

(72) Vojvodic, A.; Hinnemann, B. Nørskov, J. K. Magnetic edge states in ${\text{MoS}}_{2}$ characterized using density-functional theory. *Phys. Rev. B* **2009,** *80*, 125416.

(73) Li, Y.; Zhou, Z.; Zhang, S. Chen, Z. MoS2 Nanoribbons: High Stability and Unusual Electronic and Magnetic Properties. *J. Am. Chem. Soc.* **2008,** *130*, 16739.

(74) Solin, S. A. Ramdas, A. K. Raman spectrum of diamond. *Phys. Rev. B* **1970,** *1*, 1687.

(75) Kresse, G. Hafner, J. Ab initio molecular dynamics for open-shell transition metals. *Phys. Rev. B* **1993,** *48*, 13115.

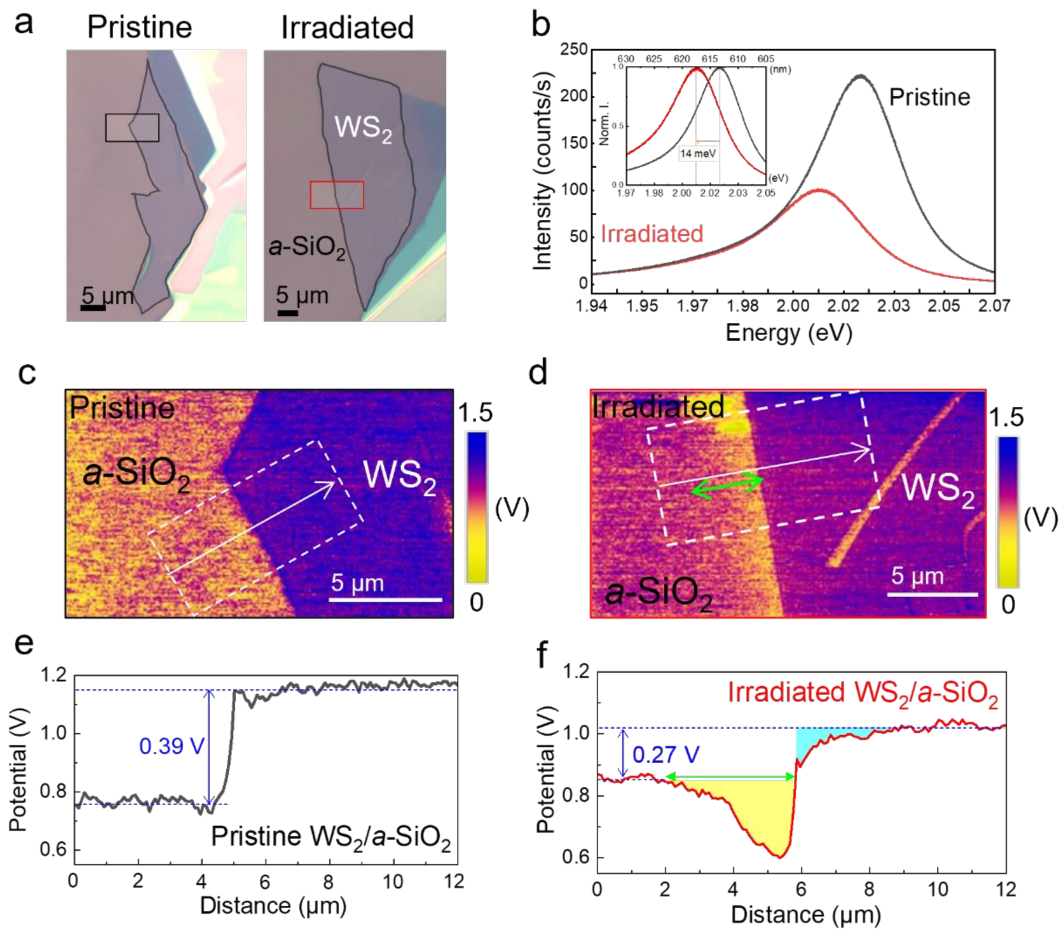

Figure 1 (a) Microscopic images of pristine WS_2 and proton irradiated WS_2 transferred onto a Si substrate with 285 nm-thick *a*-SiO_2. (b) Room temperature PL spectra of pristine (black) and irradiated WS_2 (red) on *a*-SiO_2/Si. Inset shows the normalized intensity profile at the peak position. (c,d) KPFM mapping, (e,f) areal contact potential difference (CPD) profile of pristine 1L-WS_2 (black) and proton irradiated 1L-WS_2 (red) on *a*-SiO_2/Si.

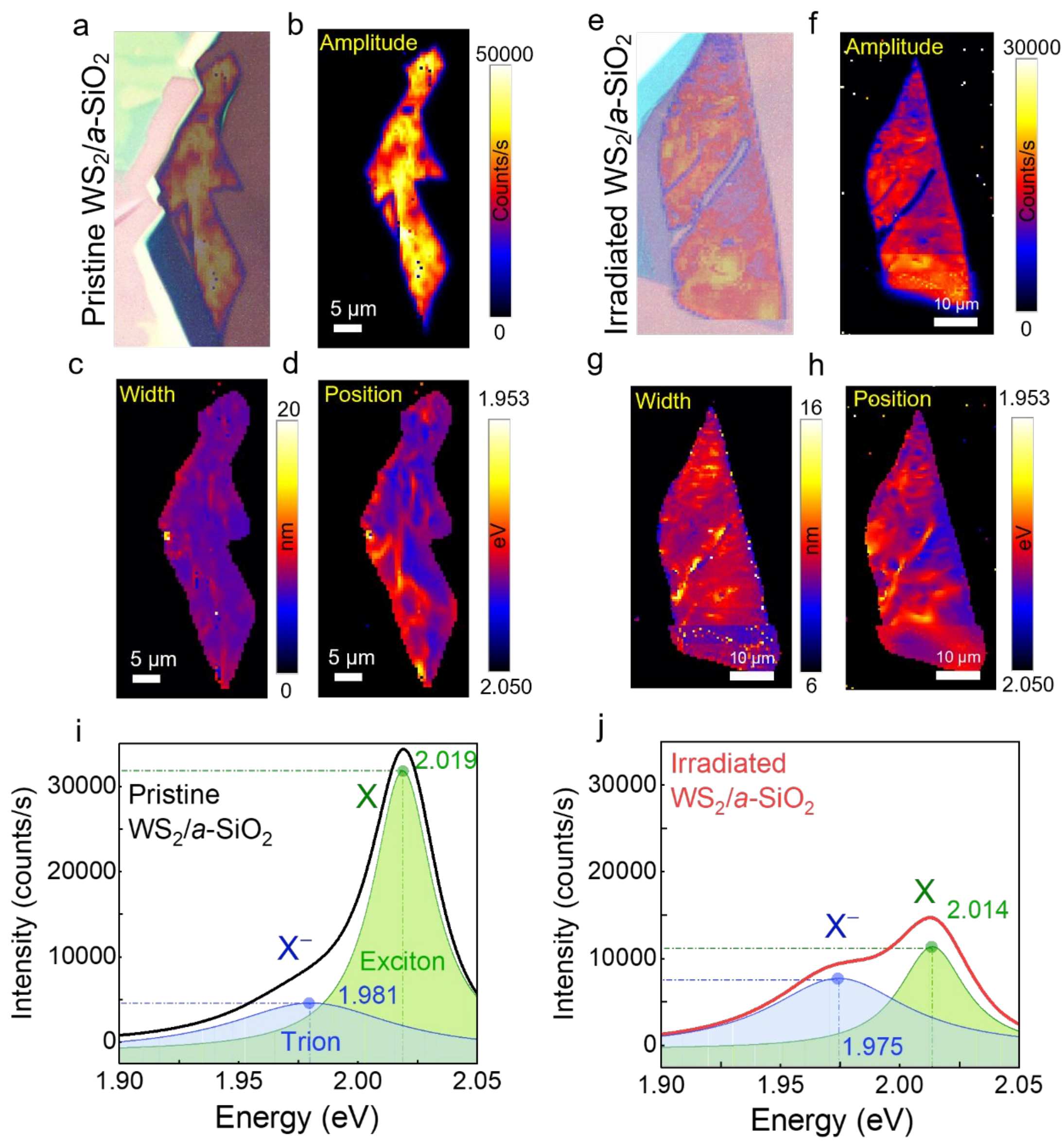

Figure 2 PL mapping. (a-d) OM image and peak amplitude (counts/s), peak width (nm) and (c) peak position (eV) mapping of pristine WS_2, (e-h) of irradiated WS_2 flake. (i,j) PL spectra of pristine WS_2 and proton irradiated WS_2. Flakes are supported by 285 nm *a*-SiO_2/Si substrate.

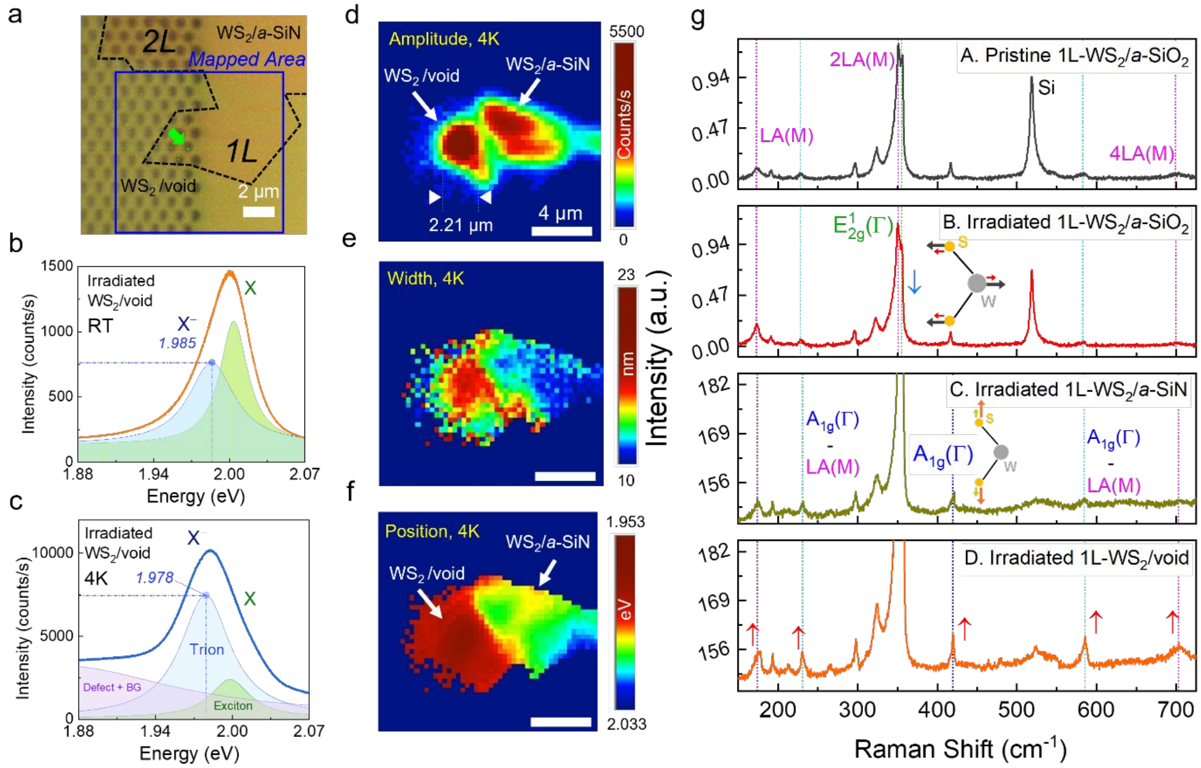

Figure 3 (a-f) PL of free-standing WS_2 after proton irradiation. (a) OM image. Black dashed area shows the transferred WS_2 flake, blue rectangle shows the region selected for PL mapping and green arrow shows the position for PL spectra collection. (b,c) PL spectra at room temperature (298 K) and at 4 K, respectively. (d-f) PL mapping of peak amplitude (counts/s), peak width (nm), and peak position (eV) at 4 K. White arrows present regions of free-standing (void) and supported (*a*-SiN) WS_2. (g) Stacked Raman spectra. A: Pristine 1L-WS_2/*a*-SiO_2, B: irradiated 1L-WS_2/*a*-SiO_2, C: irradiated 1L-WS_2/*a*-SiN, D: irradiated 1L-WS_2/void. Colored dot lines indicate Raman active modes. Blue: A_{1g}, cyan: $A_{1g} \pm$ LA modes, pink: LA modes, green: E_{2g}^1 mode. Insets illustrate atomic vibrations of E_{2g}^1 and A_{1g}.

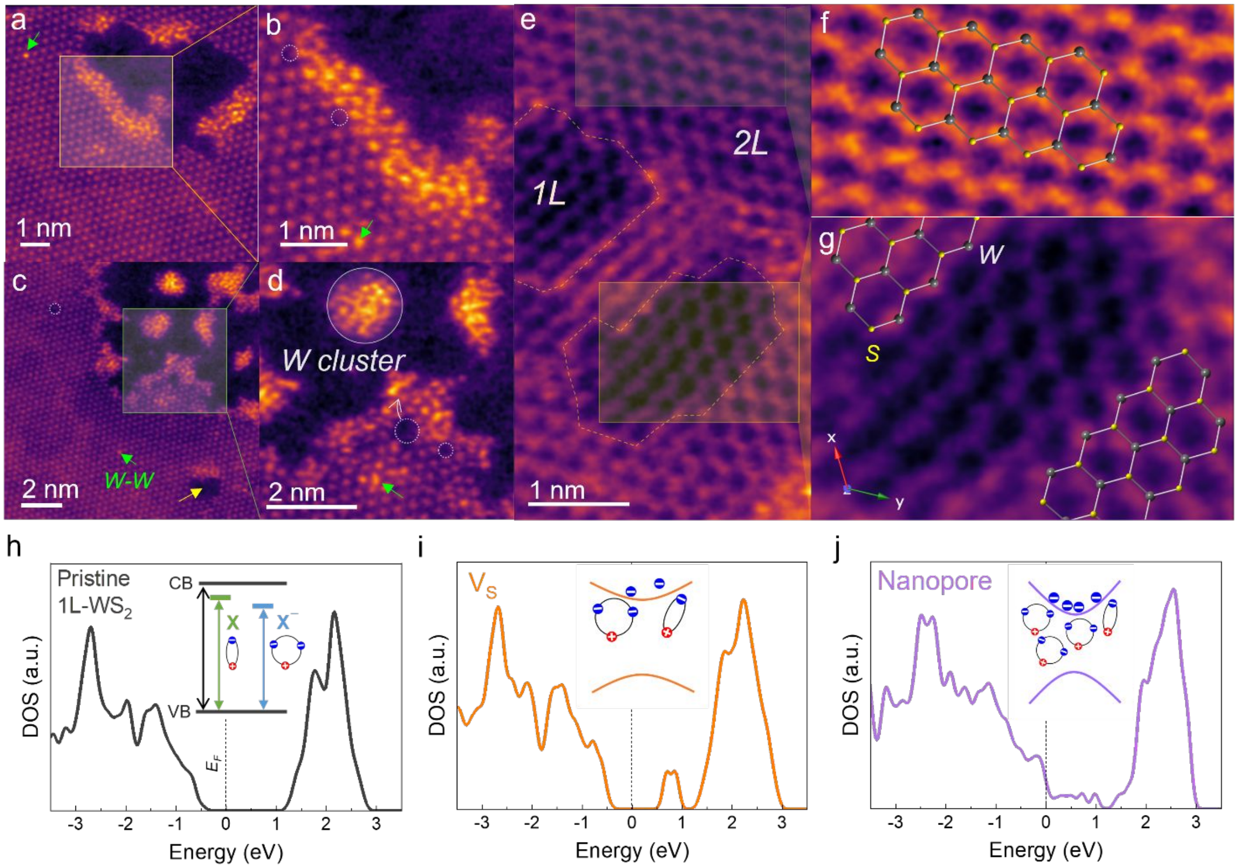

Figure 4 (a-d) HAADF HRSTEM micrographs and zoomed view of irradiated 1L-WS_2 with nanopores. Defects include atomic displacement (disorder), formation of W nanoclusters, W vacancies, and folded W-W. (e) HAADF STEM micrograph at a bilayer WS_2 region showing nanopores. (f) Atomic arrangement of WS_2 away from the nanopore, (g) at the nanopore edge. (h-j) DOS profile of pristine monolayer (black), single W vacancy (orange), nanopore with WS_2 stoichiometry (purple). Insets illustrate excitation energy of excitons and trions, predicted band structure of pristine 1L-WS_2, 1L-WS_2 with S vacancies, and 1L-WS_2 with nanopores.

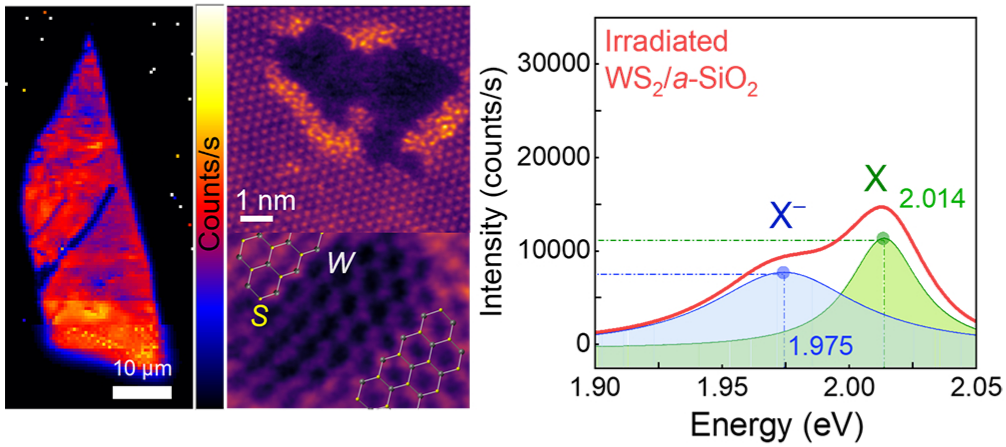

84x47mm (300 x 300 DPI)